PHYSICAL REVIEW A **103**, 032804 (2021)

Toward a description of electron-induced dissociative excitation in H_2O^+: Investigation of three resonances above the $\tilde{B}$ state

I. Rabadán [*]
Departamento de Química, Módulo 13, Universidad Autónoma de Madrid, 28049 Madrid, Spain

J. D. Gorfinkiel [†]
School of Physical Sciences, The Open University, Walton Hall, MK7 6AA Milton Keynes, England, United Kingdom

(Received 25 September 2020; accepted 9 February 2021; published 4 March 2021)

Electron-induced dissociative excitation (DE) is a little studied process of significant applied relevance. Our aim is to provide a theoretical counterpart to earlier experiments [M. J. Jensen, R. C. Bilodeau, O. Heber, H. B. Pedersen, C. P. Safvan, X. Urbain, D. Zajfman, and L. H. Andersen, Phys. Rev. A **60**, 2970 (1999)] on DE of H_2O^+. For this purpose, we have performed low-energy fixed-nuclei scattering calculations, based on the R-matrix method, for over 1800 geometries of H_2O^+. We have identified and characterized three resonances lying above the second ($\tilde{B}$) excited state of H_2O^+; their energy, lifetime, and associated quantum defect have been determined. We assess their possible contribution to the DE process.

DOI: 10.1103/PhysRevA.103.032804

I. INTRODUCTION

Molecular ions are important species in cold regions of astrophysical, planetary, and cometary environments as well as man-made plasmas. In those environments, electron collisions with molecular ions can lead to the production of hot (kinetically rich) species by dissociative recombination (DR) as well as the fragmentation of the target ions through dissociative excitation (DE). While DR has been widely studied both theoretically and experimentally, albeit for simple ions, there are very few studies devoted to DE. This latter process, however, also contributes reactive species to the medium, not only when the target is a cation but also for neutral molecules, and is therefore of relevance in other environments (e.g., irradiated biological matter where this process can lead to the formation of, for example, highly reactive OH radicals known to damage DNA [1]). The scarcity of experimental or theoretical studies of DE for neutral targets is also apparent (see [2] for a review of data for oxygen containing molecules, [3,4] for CH_4, and [5] for simplified calculations for NF_x targets), but interesting mechanisms have been identified: the electron can act as a catalyst and induce (without long-term attachment) the breakup of one or more bonds in a process named "bond-breaking by catalytic electron" [6] observed, for example, in formic acid [7].

One of the few experimental studies that investigate DE is the ASTRID experiment of Jensen *et al.* [8] on H_2O^+ and HDO^+ that, by measuring the energy deposited by the neutrals into the detector, was able to separate events produced by DR and DE. DE can take place via excitation into an excited cationic state or via the formation of an electronic resonance (temporary neutral state) and eventual autodetachment of the scattering electron. In both cases, the dissociation can proceed directly in the state that has been accessed (i.e., when the state formed, cationic or resonant, is dissociative *for the geometry in which it is accessed*) or via its coupling to a dissociative state (i.e., through a conical intersection or nonadiabatic coupling). Therefore an accurate modeling of the DE process, even in the lower-energy range, requires considering a number of states of the cation as well as, potentially, the large number of resonances (metastable states of H_2O) that decay into these cationic states and how the nuclear wave packet evolves on all these (coupled) potential-energy surfaces (PESs). Our initial aim is, therefore, to provide qualitative insight into the experimental results and quantitative data for the resonances that may play an important role.

In order to do this, we have carried out R-matrix calculations for electron-H_2O^+ collisions for over 1800 geometries of the cation using the UKRmol+ suite [9]. We have obtained cross sections for excitation into the lowest excited ($\tilde{A}$) and predissociating ($\tilde{B}$) states of H_2O^+ as well as resonance data. To our knowledge, the only prior literature on electron interaction with H_2O^+ is the experimental work of Mul *et al.* [10], the ASTRID experiment of Jensen *et al.* [8] already mentioned, the CRYRING experiments [11–13], the experiment of Fogle *et al.* [14] on ion production, and the theoretical work on DR of Nkambule *et al.* [15].

From our calculations, we have selected for a detailed study three Feshbach resonances that lie just above $H_2O^+(\tilde{B})$ and could influence the short-time DE fragmentation dynamics on this state and lower-energy cation states. These resonances are well separated from any others at equilibrium geometry, making their characterization easier. Investigating these resonances will enable us to establish the potential importance of the resonant contribution to DE as well as help us characterize more generally the Rydberg series they belong to.

---

[*] ismanuel.rabadan@uam.es

[†] jimena.gorfinkiel@open.ac.uk

2469-9926/2021/103(3)/032804(11)

The paper is organized as follows. Section II summarizes the R-matrix approach as applied to electron-molecule scattering in the fixed-nuclei (FN) approximation. Section III describes the characteristics of the calculation we have performed. Our results are presented in Sec. IV together with a discussion of the DE process that takes advantage of the recent studies by Suárez *et al.* [16,17] on the fragmentation of the $\tilde{B}$ state of H_2O^+. Finally, in Sec. V we summarize our conclusions and future plans for the study of DE of H_2O^+.

II. R-MATRIX THEORY

We have performed the scattering calculations using the UKRmol+ suite [9] (versions 2.0.2 of ukrmol-in [18] and 2.0.1 of ukrmol-out [19]) of codes that implement the R-matrix method [20] within the FN approximation.

The underlying idea of the R-matrix method is the division of space into two regions, inner and outer, separated by a sphere of radius a, known as the R-matrix sphere. In the inner region, correlation and exchange effects between all electrons are significant and so must be taken into account. In the outer region, these interactions can be neglected and the problem to solve becomes much simpler. It is crucial for the applicability of the method that a is chosen so that the R-matrix sphere contains the charge densities of the relevant target electronic states and the $N+1$ electron functions χ_i defined below.

In the inner region, the target + scattering electron system is described using a set of basis functions Ψ_k of the form

$$\Psi_k = \mathcal{A}\sum_{i=1}^{n}\sum_{j=1}^{n_c}\Phi_i(\mathbf{x}_N;\hat{r}_{N+1};\sigma_{N+1})\frac{u_{ij}(r_{N+1})}{r_{N+1}}a_{ijk} + \sum_{i=1}^{m}\chi_i(\mathbf{x}_{N+1})b_{ik} \tag{1}$$

where $\mathcal{A}$ is the antisymmetrization operator; Φ_i are wave functions describing the target electronic state i and the angular and spin behavior of the scattering electron; and $\mathbf{x}_N$ and $\mathbf{x}_{N+1}$ represent spin and space coordinates of all N and $N+1$ electrons, respectively. σ_{N+1} stands for the spin of the $(N+1)$th scattering electron, and r_{N+1} and $\hat{r}_{N+1}$ stand for its radial and angular coordinates, respectively. The functions $r_{N+1}^{-1}u_{ij}(r_{N+1})$ describe the radial part of the wave function of the scattering electron and the L^2 integrable functions χ_i provide the description of the short-range polarization-correlation effects; n is the total number of target electronic states included in the expansion, n_c is the number of continuum orbitals, and m is the number of L^2 functions used, that depends on the choice of model [9]. Finally, diagonalization of the inner region nonrelativistic Hermitian Hamiltonian of the $(N+1)$-electron system [20] produces the coefficients a_{ijk} and b_{ik}.

In the outer region, the computational cost of the calculations is significantly reduced as the wave function describing the scattering electron is approximated by a single-center, partial wave expansion. Having determined the basis functions Ψ_k defined by Eq. (1), the R-matrix is built at the boundary between regions and propagated to an asymptotic distance, where the K matrix is obtained by matching to asymptotic expressions for the radial wave function of the scattered particle. From the K matrix, one can determine the S matrix and, from it, the cross sections. Both K and S matrices can be used to identify and characterize resonances, by calculating the eigenphase sum from the former or the time delay matrix **Q** [21] from the latter. In this way, the resonance position, $E_{\rm res}$, and width, Γ, can be determined. Alternatively, the resonances can be parametrized using quantum defects, δ, and resonance widths, Γ. Quantum defects are obtained from $E_{\rm res}$ and the parent ion energy (E_p) through the Rydberg equation (in atomic units):

$$\delta_l = n - [2(E_p - E_{\rm res})]^{-1/2} \tag{2}$$

where n is the principal quantum number of the Rydberg electron in the dominant electronic configuration of the resonance.

In this paper, $E_{\rm res}$ and Γ have been obtained mainly by fitting the eigenphase sum around the resonance to a Breit-Wigner form using the program RESON [22]. For some geometries, it has been necessary to resort to fitting the largest eigenvalue of **Q** to the typical Lorentzian profile [21]:

$$q_{ii}(E) = \frac{\Gamma}{(E - E_{\rm res})^2 + \Gamma^2/4}. \tag{3}$$

From the corresponding eigenstate of **Q**, one can also obtain the decaying branching ratios of the resonance into the target states.

III. CALCULATION DETAILS

The water cation in its ground-state equilibrium geometry belongs to the C_{2v} point group. Its dipole moment has been calculated to be somewhat higher than 2 D, bigger than that of neutral water (measured to be 1.85 D); its calculated polarizability is, as expected, smaller: about half that of the neutral.

Our target model aims at describing with high precision the ground and the two first excited states of H_2O^+, which are well studied and known to be involved in the photodissociation of water [23], for a range of molecular geometries. In order to best describe all these states, state-averaged CASSCF orbitals were obtained with MOLPRO [24].

In order to determine an optimal target model, a number of basis sets (cc-pVDZ, cc-pVTZ, cc-pVQZ, DZP, and TZP), two active spaces [(7,9) and (7,10)], and different averaging sets of states (including between one and five states of the symmetries $^2A_1$, $^2B_1$ and $^2B_2$ were tested for the equilibrium geometry.

The model we have chosen uses the TZP basis set [25] for oxygen and the DZP [26] one for H. It includes, in the state averaging, two $^2B_1$ states (the symmetry of the ground state of H_2O^+), two $^2A_1$ states, and one $^2B_2$ state. In generating the configurations in which the electronic wave functions Φ_i are expanded, the two $1s$ electrons of oxygen are kept frozen (the corresponding molecular orbital is the $1a_1$) and the (7,10) active space consists of the following orbitals: 2-6 a_1, 1-2 b_1, and 1-3 b_2. A total of 11 target states, ten of them doublets and a quartet, were included in the scattering calculations. Table I summarizes the excitation thresholds we obtain for the six lowest states among these. The agreement with multireference configuration-interaction (MRCI) [16] results is very good with the largest difference, for the second excited state, smaller than 0.2 eV. Our calculated dipole moment is 2.13 D.

TABLE I. H_2O^+ ground-state energy (in Hartree) and excitation thresholds, in eV, at the experimental [27] equilibrium geometry of $H_2O^+(\tilde{X}\ {}^2B_1)$ ($r_{\mathrm{OH}} = 1.89\ a_0$, $\alpha = 109.3^\circ$), calculated at CAS level with basis sets TPZ/DPZ (for oxygen and hydrogen, respectively) and cc-pVTZ, together with results from multireference configuration-interaction (MRCI) calculations.

	CAS		MRCI	
State	TZP/DZP	cc-pVTZ	TZP/DZP	cc-pVTZ
$\tilde{X}\ {}^2B_1$	−75.7536	−75.7598	−75.8644	−75.8753
$\tilde{A}\ {}^2A_1$	2.030	2.024	1.996	2.005
$\tilde{B}\ {}^2B_2$	6.448	6.433	6.296	6.308
$\tilde{a}\ {}^4B_1$	12.414	12.376	12.525	12.506
$\tilde{C}\ {}^2B_1$	13.826	13.755	13.850	13.798
$\tilde{D}\ {}^2a_1$	14.005	13.961	13.979	13.938

Also included in the table are the results for the cc-pVTZ basis set (with the remaining model parameters the same): the differences in the ground-state energy and excitation thresholds are very small.

The scattering calculation used an R-matrix radius of 13 a_0 and a GTO-only continuum description. Only L^2 configurations of the type $(\mathrm{CAS})^{N+1}$ were used to describe the short-range correlation or polarization effects [9]. Partial wave expansions with $l_{\max} = 4$ and $l_{\max} = 6$ were tested for the equilibrium geometry: the effect of including two additional partial waves is very small but noticeable in the cross sections, and negligible for the resonances (see Figs. 1 and 2), so the calculations for other geometries were carried out with $l_{\max} = 4$. Other tests were performed to assess the effect on the resonances of interest. Note that in the forthcoming sections, we use the irreducible representations of the point group C_s to label both the cationic states and the resonances: this is the point group the molecule belongs to for most of its nonequilibrium geometries.

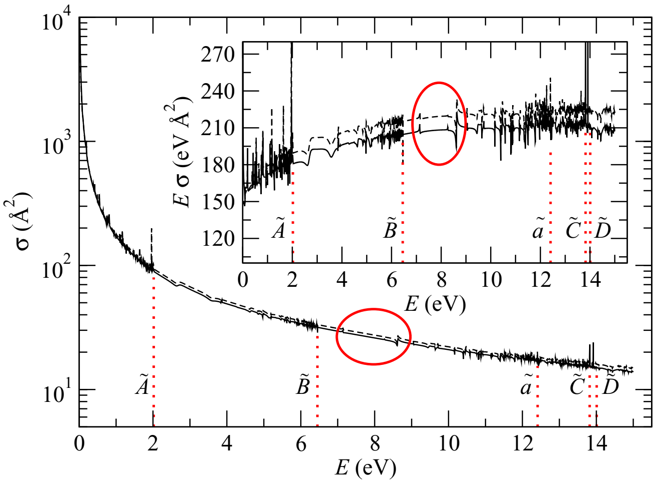

FIG. 1. Elastic cross sections for electron scattering from $H_2O^+(\tilde{X})$ at its experimental [27] equilibrium geometry. Solid lines, calculations with $l_{\max} = 4$; dashed lines, $l_{\max} = 6$. Vertical dotted lines mark the position of the electronic excitation thresholds for states $\tilde{A}$, $\tilde{B}$, $\tilde{a}$, $\tilde{C}$, and $\tilde{D}$. The inset displays the same cross sections, but scaled with the energy. Ellipses encircle the resonances under study in Sec. IV B.

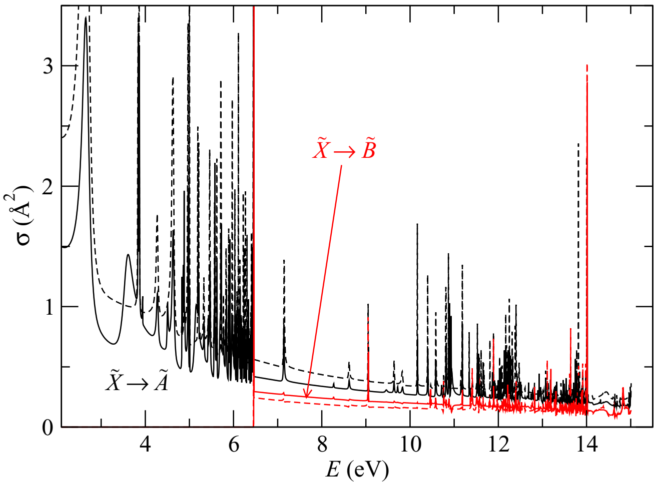

FIG. 2. Electron impact excitation cross sections from $H_2O^+(\tilde{X})$ to $H_2O^+(\tilde{A})$ (black line) and $H_2O^+(\tilde{B})$ (red line) at geometry gI. Solid lines, calculations with $l_{\max} = 4$; dashed lines, $l_{\max} = 6$.

IV. RESULTS AND DISCUSSION

We start our description and discussion of results by presenting the elastic and inelastic cross sections at the equilibrium geometry of $H_2O^+(\tilde{X})$: we locate the lowest resonances above the $\tilde{B}$ state of H_2O^+ that could be reached in electron collisions with $H_2O^+(\tilde{X})$. $\tilde{B}$ is the third electronic state of H_2O^+ and appears as a broad band, made of broad vibrational peaks, in the photoelectron spectra of H_2O [28], which points to the predissociating character of most of its vibrational states.

In Sec. IV B, we explore a large set of target geometries to characterize (determine position and width) the three lowest resonances. This set of data could be used in future dynamical studies of the fragmentation of H_2O^+, as discussed later on.

A. Scattering data at equilibrium geometry

Figure 1 shows the elastic cross section for electron collisions with $H_2O^+(\tilde{X})$ at its experimental [27] equilibrium geometry (geometry gI, henceforth) with bond length, $r_{\mathrm{OH}} = 1.888\ a_0$, and bond angle $\alpha = 109.3^\circ$. As expected for a polar target in the FN approximation, the cross section grows rapidly (roughly as E^{-1}) as the scattering energy approaches zero. The structure due to resonances is clearly visible below the excitation thresholds of states $\tilde{A}$, $\tilde{B}$, $\tilde{a}$, $\tilde{C}$, and $\tilde{D}$ marked in the figure (the next threshold in our calculations lies above 15.5 eV). The inset of Fig. 1 shows the scaled elastic cross section $E\sigma$. The first three peaks above threshold $\tilde{B}$ (encircled with an ellipse) are almost certainly the first members of the resonance series converging to states $\tilde{a}$, $\tilde{C}$, and $\tilde{D}$ and are the ones that will be studied in detail in the following section. Since here we are mainly interested in resonance properties, no attempt at approximately including (using, for example, the Born approximation) additional partial waves in the cross section has been made. The figure shows the results including

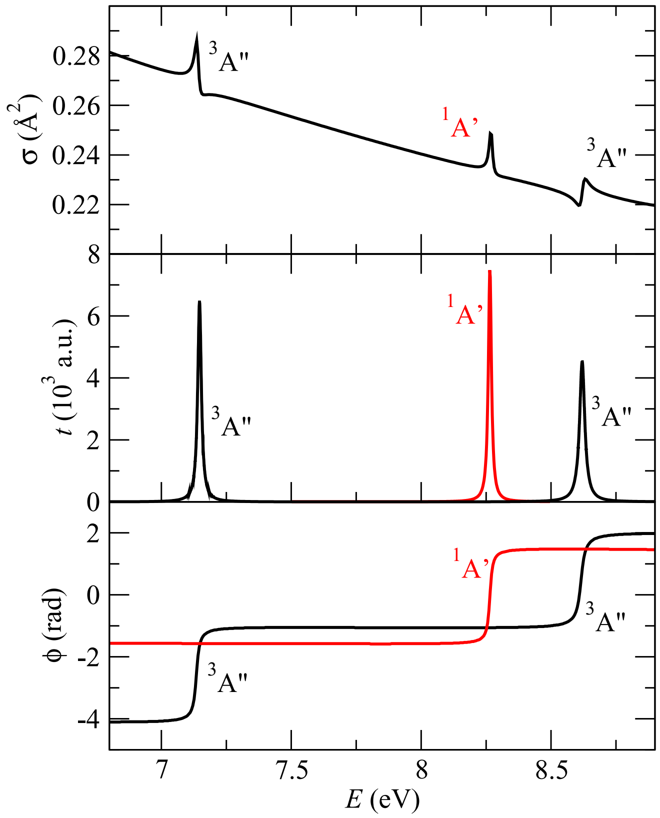

FIG. 3. Cross section for excitation into state $\tilde{B}$ (top) and time delay (middle) and eigenphase sum (bottom) for the space-spin symmetries of the selected resonances (see text) as indicated, at the equilibrium geometry of $H_2O^+(\tilde{X})$, gI. Calculations with $l_{\max} = 4$.

them up to $l_{\max} = 4$ and 6 to check the effect: the contribution to the cross section from partial waves $l = 5$ and 6 increases it by about 5% but the changes to the relevant resonances are negligible.

Figure 2 shows electronic excitation cross sections from the $\tilde{X}$ state of H_2O^+ to the two lowest excited states, $\tilde{A}$ and $\tilde{B}$, also for geometry gI. The Rydberg resonance series converging to state $\tilde{B}$ is clearly visible in the $\tilde{X} \to \tilde{A}$ cross section; less clear (because of both the size of the cross sections and the energy grid used) are the resonances above the $\tilde{B}$ threshold that converge to the $\tilde{a}$, $\tilde{C}$, and $\tilde{D}$ states. Similar to the elastic cross sections shown in Fig. 1, the increase in the cross section introduced by inclusion of the $l = 5$ and 6 partial waves is below 10 and 3% for the excitation to $\tilde{A}$ and $\tilde{B}$, respectively.

The first three resonances above the $\tilde{B}$ threshold, encircled in an ellipse in Fig. 1, are fairly isolated from others (of the same symmetry), which facilitates their study and should enable us, in future studies, to neglect their coupling to neighboring resonances at least for those geometries for which they remain above the $\tilde{B}$ state. The resonances have $^3B_1$, $^1A_1$, and $^3A_2$ symmetry ($^3A''$, $^1A'$, and $^3A''$ in the C_s point group), respectively. (The first resonances of $^3A'$ and $^1A''$ symmetry appear above 9 eV). The effect of their presence on several scattering quantities (cross section, eigenphase sum, and time delay) is shown in Fig. 3. All three quantities demonstrate that, for this geometry, the resonances are well isolated and can therefore be well characterized.

TABLE II. H_2O resonance parameters (energy, E_{res}, in eV; width, Γ, in meV; and quantum defect, δ, with respect to the state in brackets) obtained with the reference (Ref.) calculation (basis set TZP/DZP, $l_{\max} = 4$, and $R = 13\ a_0$) and absolute differences with respect to the reference values obtained with either additional partial waves ($l_{\max} = 6$) or a change of basis set (cc-pVTZ), as indicated in the table.

Sym.		Ref.	$l_{\max} = 6$	cc-pVTZ
$^1A'$	E_{res} (eV)	8.265	−0.001	−0.036
	Γ (meV)	14.46	0.02	−0.30
	δ ($\tilde{D}$)	1.46	0.00	−0.01
$^3A''$	E_{res} (eV)	7.135	0.000	−0.027
	Γ (meV)	17.75	0.06	0.63
	δ ($\tilde{a}$)	1.39	0.00	0.00
$^3A''$	E_{res} (eV)	8.616	−0.003	−0.077
	Γ (meV)	24.51	0.06	−0.21
	δ ($\tilde{C}$)	1.38	0.00	0.00

A summary of the properties of these resonances for geometry gI is presented in Table II. Resonance position, width, and quantum defect were calculated with our chosen model ("reference" calculation) described in Sec. III, and are compared with values obtained either setting $l_{\max}$=6 or using the basis set cc-pVTZ. The changes in the resonance parameters are shown as absolute differences. We note that the uncertainty in these parameters, as given by the considered changes to the model, is negligible when increasing $l_{\max}$ and no bigger than 3.5% when the basis set is changed.

The branching ratios of the resonances when the captured electron is reemitted are calculated from the eigenvector coefficients of the **Q** matrix corresponding to its largest eigenvalue [21]. For geometry gI, and at the resonance energies, the values we obtain are listed in Table III. As we can see, the main decay channel for resonance $^1A'$ is into the $\tilde{B}$ state, while the $^3A''$ resonances decays mainly into the ground state. The contribution to the excitation cross section into state $\tilde{B}$ in the top panel of Fig. 3 seems to show, nonetheless, that all three resonances produce similar enhancements of this process. Comparison of the state-to-state cross sections shows that the lowest $^3A''$ resonance enhances the excitation into the $\tilde{A}$ state significantly more than to the $\tilde{B}$ state; the same is true, though to a lesser extent, for the second $^3A''$ resonance. In the case of the $^1A'$ resonance, the enhancement of both processes is similar.

TABLE III. Decaying branching ratios of the $^1A'$ and $^3A''$ selected resonances for geometry gI (see text), into H_2O^+ states $\tilde{X}$, $\tilde{A}$, and $\tilde{B}$, at the specified scattering energies.

	E (eV)	$\tilde{X}$	$\tilde{A}$	$\tilde{B}$
$^1A'$	8.264	0.289	0.266	0.444
1 $^3A''$	7.147	0.878	0.117	0.005
2 $^3A''$	8.620	0.978	0.018	0.004

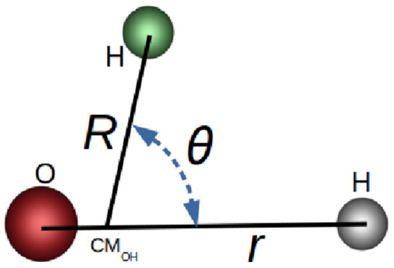

FIG. 4. Jacobi coordinates.

B. Resonance parameters as a function of cation geometry

The study of the PESs corresponding to the three resonances identified in the previous section has been carried out in the grid of points (set of geometries) used in Suárez *et al.* [17]. This grid is defined in the Jacobi coordinates $\{R, r, \theta\}$ illustrated in Fig. 4. The dependence of the lifetime and quantum defect of the three resonances has also been investigated.

Figures 5 and 6 show cuts of the PES of the three resonances together with some of the target states included in the scattering calculation: the former cuts along the Jacobi R coordinate for $\theta = 110^\circ$ and $r = 1.90\ a_0$ whereas the latter cuts along θ with R=1.98 a_0 and r=1.90 a_0. The energies of the H_2O^+ states are obtained as described in Sec. III. The soft-color stripes have been obtained from the parent ion potential-energy curves using Eq. (2) with $n = 3$ and quantum defects of $\delta = 1.40 \pm 0.05$ ($1\,^3A''$), 1.35 ± 0.05 ($2\,^3A''$), and 1.45 ± 0.05 ($^1A'$). The calculated resonance positions fall, on the whole, inside these stripes.

The first three resonances above the $\tilde{B}$ state are well isolated for many geometries and can be characterized by fitting the eigenphase sum using RESON. However, when the resonances fall below the $\tilde{B}$ threshold, identifying the correct peaks among the "forest" of spikes corresponding to the Rydberg series that converge to this state becomes more difficult. This is illustrated in the figures in the Appendix, where we show the largest eigenvalue of the time delay in the energy region of each of the three resonances of interest for different values of R.

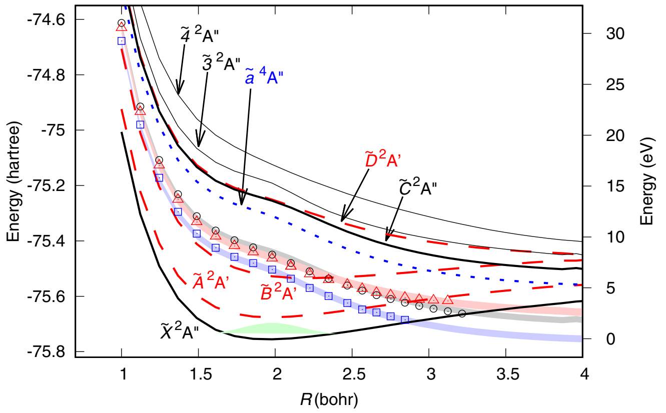

FIG. 5. Cut of the PESs along the Jacobi R coordinate with $\theta = 110^\circ$ and $r = 1.90\ a_0$. The lines correspond to electronic states of H_2O^+: $^2A''$(solid black), $^2A'$(dashed red), and $^4A''$(dotted blue). The blue squares ($1\,^3A''$), black circles ($2\,^3A''$), and red triangles ($^1A'$) correspond to the resonance positions obtained from RESON, when above state $\tilde{B}$, and the time delay method below. The blue stripe is obtained from the $\tilde{a}$ state using quantum defect theory with $1.35 < \delta < 1.45$, the gray stripe is obtained from $\tilde{C}$ with $1.3 < \delta < 1.4$, and the red stripe is obtained from $\tilde{D}$ with $1.4 < \delta < 1.5$. Target state labels are included for clarity. Also shown is the approximate ground-state vibrational wave function (green shaded area at the bottom of the $\tilde{X}$ state).

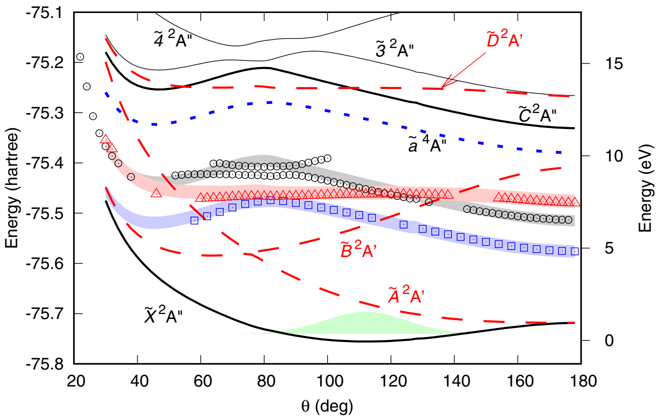

FIG. 6. Same as Fig. 5, but the cut of the PESs is along θ with $R = 1.98\ a_0$ and $r = 1.90\ a_0$. Additionally, the upper row of black circles corresponds to a higher resonance of $^3A''$ symmetry, included to show its avoided crossing with the $2\,^3A''$ resonance.

We can see in Figs. 5 and 6 that, overall, the resonance curves follow those of their corresponding parent states: the lower $^3A''$ resonance follows that of the $\tilde{a}$ state, the $^1A'$ resonance follows that of the $\tilde{D}$ state, and the second $^3A''$ resonance follows that of the $\tilde{C}$ state; this is particularly obvious in the PES cut along the angular coordinate, shown in Fig. 6, where the curves have clearly different shapes. In this figure, we see that the three resonances are below the $\tilde{B}$ state for $50^\circ > \theta > 140^\circ$, while in Fig. 5, the resonances are below $\tilde{B}$ for $R > 2.3\ a_0$. In the case of the $2\,^3A''$ resonance, Fig. 6 shows that in the region around 80°, where states $\tilde{C}$, $3\,^2A''$, and $4\,^2A''$ have several avoided crossings, its energy curve does not follow that of state $\tilde{C}$ (neither adiabatically nor diabatically).

The resonance PESs are repulsive in the R and r coordinates around the equilibrium geometry of H_2O^+, so the capture of one electron into them will trigger the stretching of both O-H bonds. If the resonances decay into the $\tilde{B}$ state, the remaining cation can dissociate as shown by Suárez *et al.* [17], but if the resonance survives long enough to reach geometries where it can only decay into $\tilde{A}$ or $\tilde{X}$, then the dissociation of the cation will depend on the amount of electronic energy that is converted into nuclear kinetic energy.

The original set of geometries in Suárez *et al.* [17] contained 278 382 points. Here, we choose a subset of these geometries for which the resonances are above state $\tilde{B}$, as estimated using the fact that, as seen above, the positions of the resonances can, in general, be approximated by a small range of geometry-independent values of quantum defect. This leads us to consider geometries with $R \in [1.0\,a_0; 2.4\,a_0]$, $r \in [1.3\,a_0, 2.4\,a_0]$, and $\theta \in [10^\circ, 179^\circ]$. Our results are illustrated in Fig. 7.

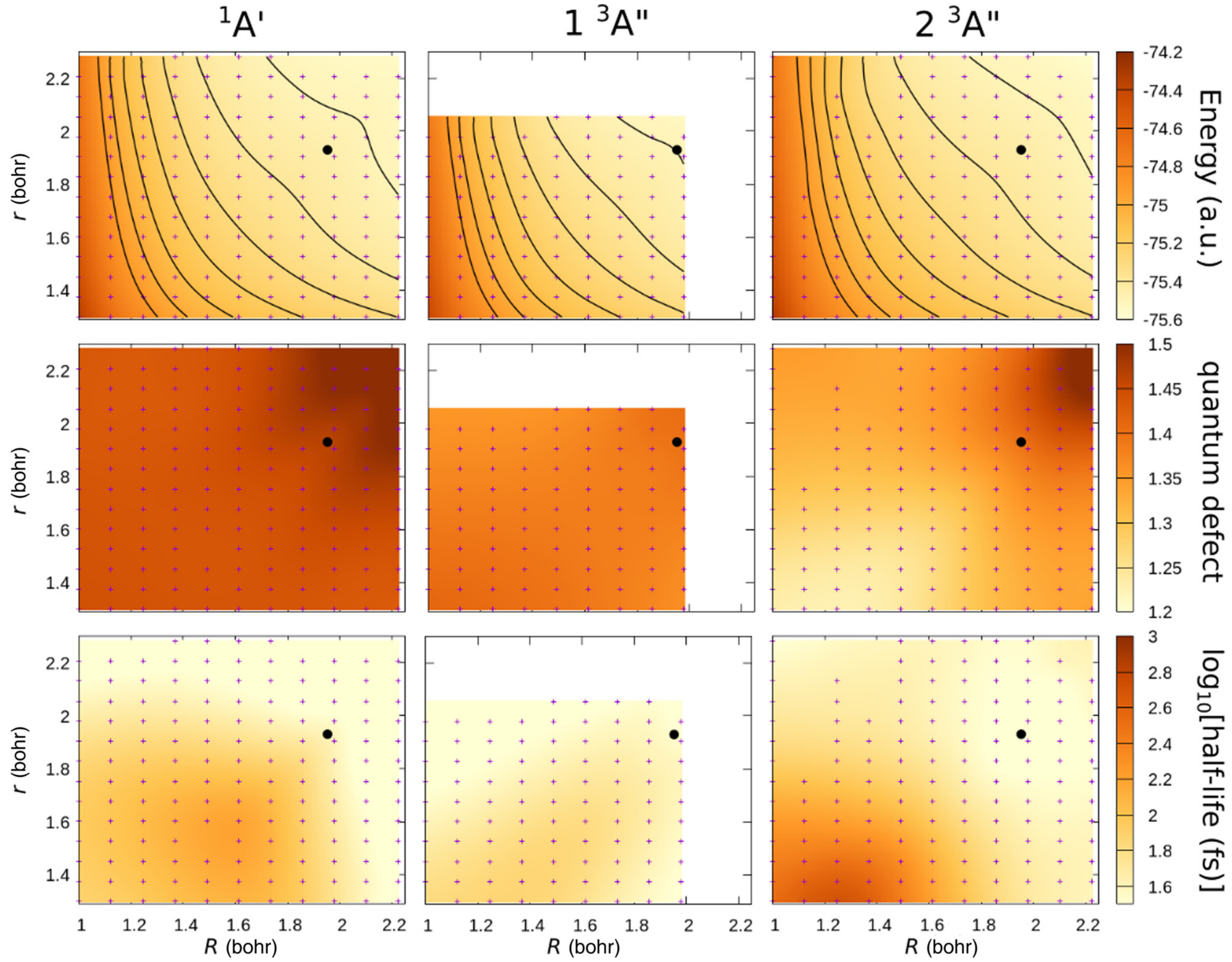

FIG. 7. Color maps of the PES (in Hartree), quantum defects, and the logarithm of half-life in fs of the ${}^1A'$, $1\ {}^3A''$, and $2\ {}^3A''$ resonances as a function of the Jacobi coordinates r and R for $\theta = 110^\circ$. The scale of the color map for each magnitude is indicated on the right. The light dots in all panels indicate the geometries for which the quantities have been obtained; the bullet indicates the ground-state equilibrium geometry of the cation; the black lines in the energy panels are isoenergetic lines obtained from a 2D cubic spline interpolation. The white bands in the panels for resonance $1\ {}^3A''$ correspond to geometries where this resonance is below state $\tilde{B}$.

The three upper panels of Fig. 7 show the contour plot of the ${}^1A'$ (left), $1\ {}^3A''$ (center), and $2\ {}^3A''$ (right) resonance energies as a function of the Jacobi coordinates r and R for θ=110°, in the region where their energies are above that of state $\tilde{B}$. The light dots mark the geometries where the resonances have been successfully fitted; the lines join values with the same energy, which is otherwise indicated with a color map on the right-hand side. A bullet in all panels marks the the equilibrium geometry of $H_2O^+(\tilde{X})$. As we see, the three PESs are repulsive in the coordinate space depicted. This means that when H_2O^+ captures an electron in any of these resonances, the neutral system will evolve by stretching out both O-H bonds until it decays to an electronic state of H_2O^+, or it dissociates into neutral fragments (DR).

The three central panels in Fig. 7 show the quantum defects, δ, of the resonances depicted using the color map on the right. As mentioned before, the quantum defects are obtained using Eq. (2) with $n = 3$, the resonant energy shown in the upper panels, and the energy of the corresponding parent state ion. For the same geometries, the bottom three panels in Fig. 7 show the lifetime (or half-life, $\tau = \hbar/\Gamma$) of the resonances. The lifetimes are about 40 fs for the resonance ${}^1A'$, 35 fs for $1\ {}^3A''$, and 25 fs for $2\ {}^3A''$, around the Frank-Condon geometries, and decrease when either of the two coordinates r or R increases. These half-lives are sufficient to allow nuclear motion before the electron is reemitted (autodetachment), and indeed the system could reach geometries where resonance decay is no longer possible and DR is inevitable.

A similar cut to that in Fig. 5, but for the quantum defect and half-life of the resonances, is shown in Fig. 8. Here we can appreciate the relative low variability in the values of the quantum defect of the resonances, particularly for the $1{}^3A''$ one, even when crossing below the $\tilde{B}$ threshold ($R > 2.3\ a_0$). We suggest that at least the two lower resonances could be included in dynamics simulations using a single value quantum defect for all the geometries. With respect to the

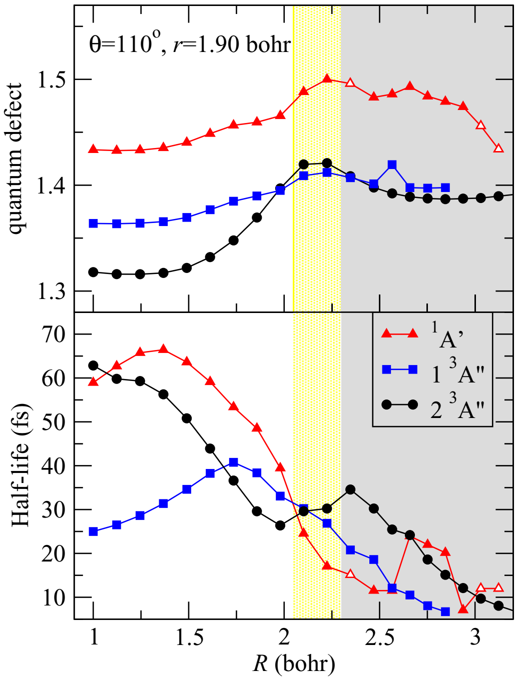

FIG. 8. Quantum defect and half-life along a cut of PES with fixed $\theta = 110^\circ$ and $r = 1.90\ a_0$. The yellow area corresponds to geometries where only the $1\ ^3A''$ resonance is below the $\tilde{B}$ threshold, while in the gray area the three resonances are below the $\tilde{B}$ threshold. White-filled triangles correspond to the tentative fittings of hidden resonances (see Fig. 9).

resonance half-life, we see the dependence with geometry is more marked.

C. Discussion

The main aim of investigating the resonances described above is to understand their potential contribution to DE and generate the data required for future nuclear dynamics calculations. In this section we discuss the DE experimental results of Jensen *et al.* [8] for the lower range of energies investigated, in order to understand how their results can be analyzed using current knowledge of electron-H_2O^+ collisions and dissociation dynamics in the $\tilde{B}$ state and to motivate future calculations.

Jensen *et al.* [8] provide absolute cross sections for the production of different neutral fragments via DE in the electron scattering energy range of 1–50 eV. The dissociation energy of $H_2O^+(\tilde{X})$ is about 5.1 eV: the experiment seems to detect DE signal below this threshold. However, the uncertainty in the measurements is larger than the measured cross sections, so these values should be interpreted extremely carefully. $H_2O^+(\tilde{A})$ has a dissociation energy of about 4.2 eV, which also rules out its contribution to fragmentation at 4 eV and below. On the other hand, $H_2O^+(\tilde{B})$, which only supports two bound vibrational levels, can easily dissociate above 0.3 eV via a conical intersection that populates states $\tilde{A}$ and $\tilde{X}$; for energies above 2.7 eV, dissociation directly on the $\tilde{B}$ PES is also possible [17].

The channels $H + OH^+$ and $OH + H^+$ [29] lead to the largest DE cross sections for almost the whole energy range. The ratio of the cross sections for each of these to the sum of both (i.e., neglecting the other two channels, $O + H_2^+$ and $2H + O^+$) can be directly compared to that obtained by Suárez *et al.* [17] from nonadiabatic quantum dynamics calculations of the predissociation of the $\tilde{B}$ state. Intriguingly, these ratios are very similar at 2 eV (and also consistent with earlier ionization measurements [30]). Above ≈5.0 eV, the fragmentation ratios from Jensen *et al.* [8] abruptly change and the production of H/OH^+ is boosted over that of OH/H^+. Further, the cross sections show that, while the production of OH/H^+ increases approximately linearly with energy, in the ≈ 6–9-eV energy range, that of H/OH^+ is approximately constant. This constant behavior is also observed for OD^+ production from D_2O^+ by Fogle *et al.* [14] in their crossed beam measurements (D^+ was not measured in that experiment).

The lowest-energy fragmentation path for state $\tilde{X}$ leads to the production of $H + OH^+$ while state $\tilde{A}$ produces $OH + H^+$. State $\tilde{B}$ can lead to both, either directly on its own PES (for the former) or via the above-mentioned conical intersection (both). Above the threshold of state $\tilde{A}$ (here we refer to the energy required to excite state $\tilde{A}$, from state $\tilde{X}$, into the vibrational continuum, so this threshold is ≈6.0 eV) production of OH can occur via direct excitation of this state. The threshold for OH or H production via transfer from state $\tilde{B}$ through the conical intersection is closed, since around 6.3 eV is required to excite the $\tilde{B}$ state (and the zero-point energy of H_2O^+ in state $\tilde{X}$ is around 0.5 eV). The electronic (fixed-nuclei) excitation cross sections into states $\tilde{A}$ and $\tilde{B}$ are similar in size in this energy range (see Fig. 2) so without dissociation dynamics calculations it is not possible to ascertain the contribution each of these states can make to the DE cross section.

The abrupt change in H production occurs between 5 and 6 eV, and so is conceivably linked to dissociation in state $\tilde{X}$ becoming energetically possible. Above around 6–6.3 eV, dissociation from state $\tilde{B}$ can also contribute to this signal. It is interesting that while the elastic electronic cross section is around two orders of magnitude larger than the inelastic cross section, the DE cross section for H is only between 0.5 and 1 times bigger than that for OH.

The fact that the H cross section remains roughly constant until ≈9–10 eV indicates that the additional energy put into the system does not lead to more DE. On the other hand, the approximately linear dependence with energy of the OH cross section in the ≈6–9-eV energy range would seem to indicate an effect related to increasing transfer of kinetic energy of the projectile into the nuclear motion of the molecule.

No additional cationic states become energetically accessible until around 14 eV. However, 8–9 eV is the region where resonances converging to the states $\tilde{C}$, $\tilde{a}$, and $\tilde{D}$ start to become significant. Indeed, our calculations show that the three resonances investigated in the 7–9-eV range in e-H_2O^+ collisions are repulsive as the O-H bond increases. Their lifetimes are long enough to allow conversion of electronic energy into kinetic energy. These resonances can contribute to DE via the resonant excitation of the cationic states. Since autodetachment does not happen instantaneously, the geometry of the cationic states into which the resonance has decayed can be different to that at which these states were accessed via direct (nonresonant) excitation.

One can estimate a survival probability for a resonance that indicates the likelihood the system will dissociate before autodetachment takes place. This probability can be expressed as $p = \exp[-\tau_D/\tau_a]$ where τ_a is the resonance lifetime (associated to autodetachment) and τ_D is the time it takes the nuclei to move from their geometry when the resonance is formed to that at which autodetachment is no longer possible (i.e., the resonance has stabilized) and dissociation (DR in this case) is therefore inevitable. In turn, if one assumes two-body breakup along the coordinate R,

$$\tau_D = \int_{R_{\rm exc}}^{R_c} \frac{dR}{v(R)}, \quad v(R) = \sqrt{\frac{2}{\mu}[E - V(R)]}, \qquad (4)$$

where $R_{\rm exc}$ is the geometry for which the excitation takes place and R_c is the geometry at which the resonance crosses below the cation state of interest, μ is the reduced mass of the products, E is the scattering energy, and $V(R)$ is the energy of the resonant state of interest. With this simple model, the estimated "DR times" are much shorter than the autodetachment lifetimes for the resonances studied in this paper. This suggests that stabilization of the resonance (below either state $\tilde{B}$ or state $\tilde{X}$) via DR is more likely to take place than DE. However, a full quantum-mechanical simulation would be necessary to confirm this.

In Jensen *et al.*'s paper [8], the cross sections for both processes at around 10 eV are of the same order of magnitude (DE being, perhaps, slightly bigger). This fact, together with the analysis of the DR times above, may indicate that the DE process occurs mainly nonresonantly (i.e., through direct excitation of cationic states). Further support for this hypothesis comes from the fact that, at equilibrium geometry, the resonant contribution to the total cross section (within the FN approximation) looks small. On the other hand, Jensen *et al.* highlight the presence of peaks in the O and H channels that could be associated with resonance formation [8] above ≈ 10 eV. We therefore believe the resonant contribution cannot be fully discarded until nuclear dynamical calculations are performed.

V. CONCLUSIONS AND PROSPECTS

We have performed R-matrix calculations for e-H_2O^+ collisions and provided elastic and inelastic cross sections at the equilibrium geometry of $H_2O^+(\tilde{X})$. We have also focused on the three lowest resonances (autoionizing states of H_2O) above the $H_2O^+(\tilde{B})$ state in this geometry and explored the three-dimensional geometry space to characterize them.

These calculations have enabled us to shed some light into the DE experiments of Jensen *et al.* [8]: the electronic excitation cross sections seem to indicate that states $\tilde{A}$ and $\tilde{B}$ are similarly populated by electron impact, with the electronically elastic process (that populates state $\tilde{X}$) being, as expected, the most likely.

The characterization of the resonances mentioned has shown that they are repulsive in the Jacobi coordinates R and r, but can have a different behavior on θ: resonance $^1A'$ is flat in the region close to the equilibrium geometry of $H_2O^+(\tilde{X})$ (gI), while the $^3A''$ resonances will drive H_2O towards larger bond angles, which runs against the fragmentation along the channel $O + H_2$. The lifetimes of the resonances are about an order of magnitude bigger than the estimated DR time, so DR is likely to be the most probable decay process for these resonances.

With regard to higher-energy resonances corresponding to the same Rydberg series as those analyzed, it is not obvious whether they are more or less likely to contribute to DE. The resonance width in a Rydberg series decreases with the principal quantum number n as $\Gamma_n = \text{const}/(n-\delta)^3$ [31]; hence, the half-lives increase with $(n-\delta)^3$, giving the resonances more time to stabilize and leading to DR. However, the time needed for the system to reach the geometries where the resonance stabilizes also grows with n (the crossing with the cationic states occurs at longer bond lengths) and the competition between these two effects will determine the fate of the system and whether DR or DE is more likely.

The next step in our studies will be to model the DE process for a couple of energies, one below the resonances discussed

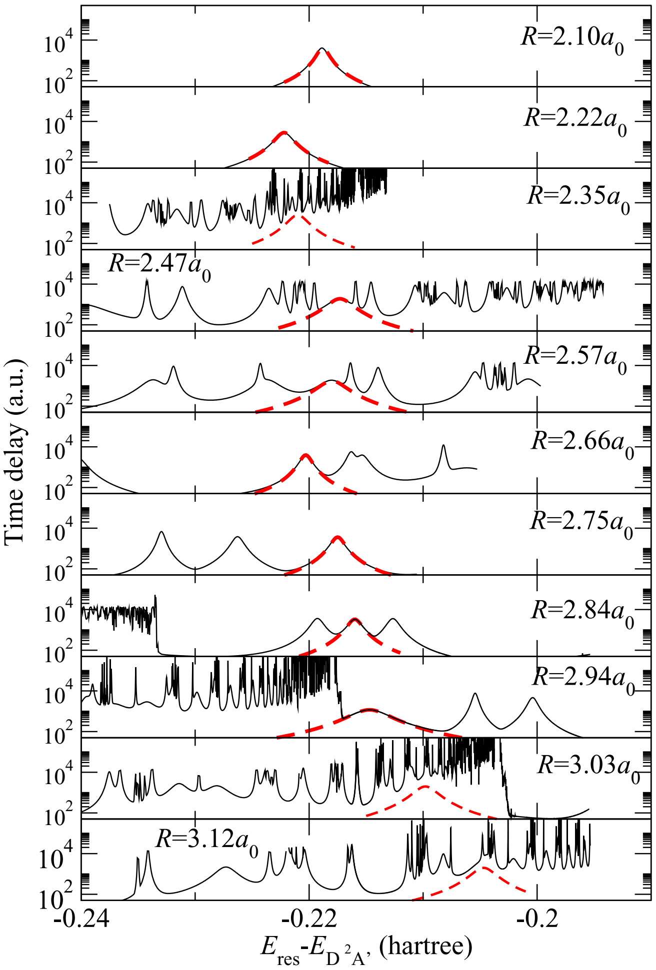

FIG. 9. Time delay for resonances of symmetry $^1A'$ for the values of the R coordinate indicated. For each panel, the zero of energy is located at the energy of the $\tilde{D}$ target state, so the resonances of the Rydberg series converging to $\tilde{D}$ appear at approximately the same energy. Red-dashed lines are drawn using the parameters plotted in Fig. 8 for resonance $^1A'$; the thin red-dashed ones are only tentative resonances and are shown with white-filled triangles in Fig. 8.

in this paper and one in the energy region where they could play a role, to shed more light on the results of Jensen *et al.* [8]. Initial calculations will exclude the resonance contributions but take into account the dynamics on the coupled PES of the cationic states, how these are populated by the electron collision, and the excess energy provided by it. The nuclear dynamics on the resonance PES will be investigated at a later stage.

In the longer term, we hope these studies will help us develop an approach to study DE in other targets of interest, for example, neutral water for which these cross sections are much needed [32].

The main data generated for this publication can be accessed at the Universidad Autónoma de Madrid data repository [33] and used under CC BY-NC 4.0 license.

ACKNOWLEDGMENTS

I.R. acknowledges funding by Projects No. PRX18/00445 and No. FIS2017-84684-R (Spanish Ministerio de Ciencia e Innovación). The R-matrix calculations were performed at The Open University STEM-Linux cluster. We also want to thank Prof. Andersen for a helpful discussion about the ASTRID experiment.

APPENDIX: CHARACTERIZATION OF THE RESONANCES BELOW THE $\tilde{B}$ THRESHOLD

In this Appendix we show the time delay as a function of scattering energy for different cation geometries with $\theta = 110^\circ$, $r = 1.90\ a_0$, and a range of R values indicated in the figures. The aim is to show the difficulty in characterizing the resonances, and therefore determining their position and width by fitting them to Eq. (3), when they are immersed in the Rydberg resonant series converging to the different ionic states. In order to help identify the resonance of interest at different geometries, we have shifted the energy scale so that zero corresponds to the energy of the parent state.

In Fig. 9 we show results for the $^1A'$ resonance. For $R = 2.10\ a_0$ and $2.22\ a_0$ (the two top panels) the resonance is above the $\tilde{B}$ threshold and can be easily fitted (red-dashed line). For

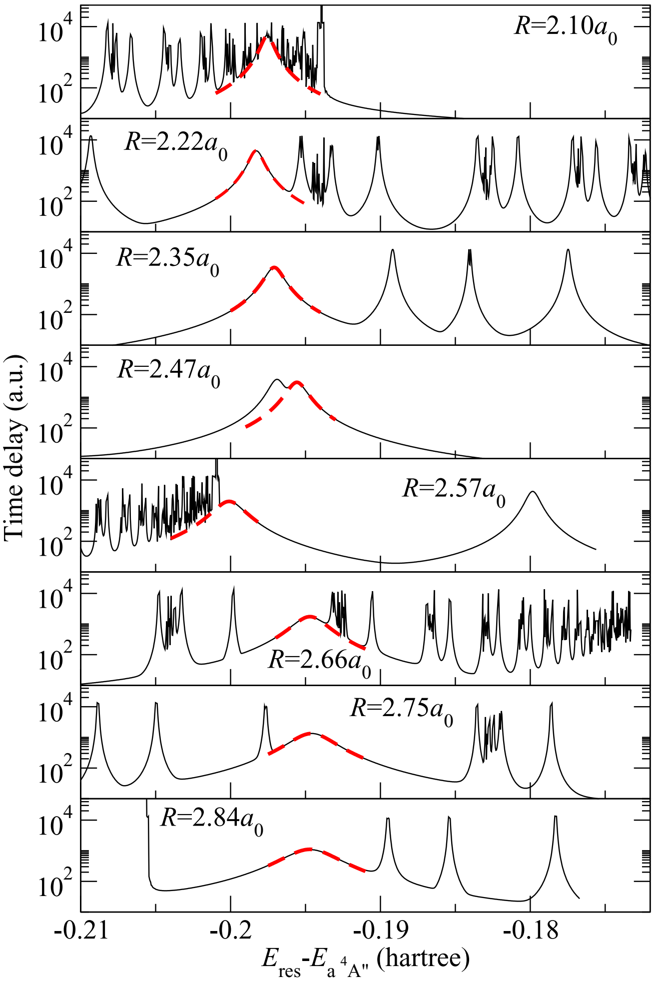

FIG. 10. Time delay for resonances of symmetry $^3A''$. For each panel, the zero of energy is located at the energy of the $\tilde{a}$ target state, so the resonances of the Rydberg series converging to $\tilde{a}$ appear at approximately the same energy. Red-dashed lines are drawn using the parameters plotted in Fig. 8 for resonance $1\ ^3A''$.

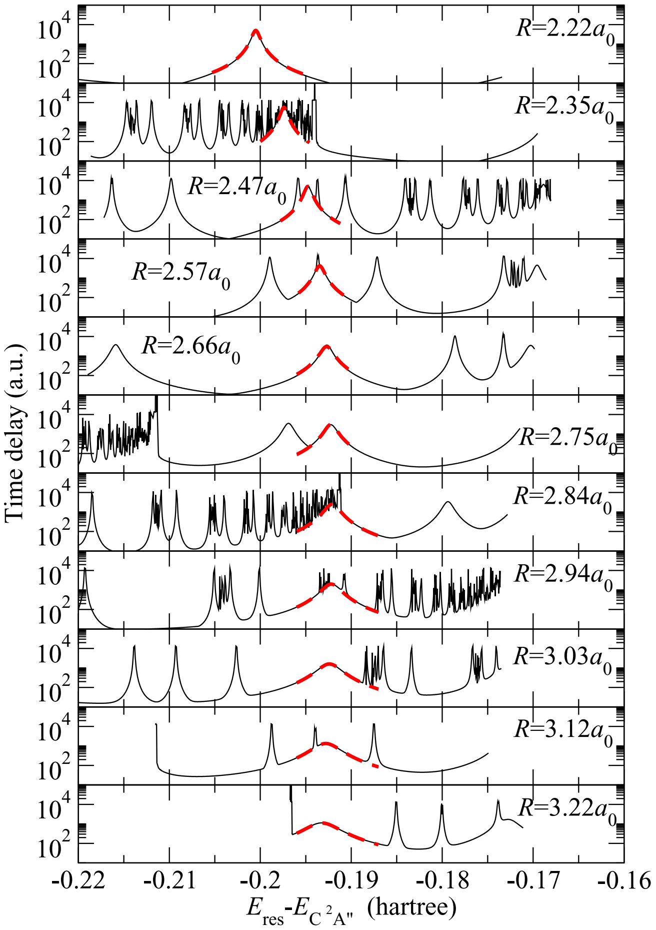

FIG. 11. Time delay for resonances of symmetry $^3A''$. For each panel, the zero of energy is located at the energy of the $\tilde{C}$ target state, so the resonances of the Rydberg series converging to $\tilde{C}$ appear at approximately the same energy. Red-dashed lines are drawn using the parameters plotted in Fig. 8 for resonance $2\ ^3A''$.

$R = 2.35\ a_0$, however, it is immersed in the resonance series converging to the $\tilde{B}$ threshold. The contribution to the time delay of these Rydberg resonances is very big so the first member of the resonance series converging to $\tilde{D}$ (the ${}^1A'$ resonance of interest) is not evident. We have tentatively included its estimated peak, determined by looking at the difference in the time delays calculated at R and $R + \delta R$ and plotted with respect to an effective quantum defect. The resonance peak is fairly straightforwardly identified between $R = 2.47\ a_0$ and $2.84\ a_0$. However, for $R = 2.66\ a_0$ there seems to be a sudden change in the resonance width (and a small bump in the quantum defect in Fig. 8); it is unclear from the time delay why this is so. The half-life of the resonance remains high, and fairly constant, in this range of R.

At $R = 2.94\ a_0$, the resonance is just above the $\tilde{A}$ threshold. For $R = 3.03\ a_0$ and $3.12\ a_0$, the resonance falls under the $\tilde{A}$ threshold and its presence could only be inferred, hidden under the peaks of the series converging to $\tilde{A}$, by looking at the time delays at R and $R + \delta R$. We have marked those tentative fittings with thin-red-dashed lines.

In the same vein, Fig. 10 shows the time delay for the ${}^3A''$ scattering symmetry as a function of impact energy measured from the $\tilde{a}$ state, in the energy region of the $1\ {}^3A''$ resonance. The top panel corresponds to $R = 2.10\ a_0$ and shows the resonance just below the $\tilde{B}$ threshold, embedded in the Rydberg series converging to it. The resonance is isolated, and so can be well characterized, at $R = 2.22\ a_0$ and $2.35\ a_0$. At $R = 2.47\ a_0$ it strongly overlaps with another resonance so it cannot be definitely assigned (we have opted for the higher peak when presenting our results). At $R = 2.57\ a_0$, the maximum of the resonance peak is just above the $\tilde{A}$ threshold; the small spike in the quantum defect in Fig. 8 seems to be linked to the crossing of the threshold. The resonance is also easily identified for $R = 2.66$, 2.75, and $2.84\ a_0$, as the Rydberg resonances converging to state $\tilde{A}$ are, on the whole, higher in energy.

Similar information is provided in Fig. 11 for the $2\ {}^3A''$ resonance, this time as a function of impact energy as measured from the $\tilde{C}$ state. For $R = 2.22\ a_0$ (top panel), the resonance is just above the $\tilde{B}$ threshold. At $R = 2.35\ a_0$, the resonance is just below it, embedded in the Rydberg series converging to the $\tilde{B}$ state. Between $R = 2.47\ a_0$ and $2.75\ a_0$, the resonance is easily identified. At $R = 2.84\ a_0$, it falls just below the $\tilde{A}$ threshold, but can still be identified. For the larger R shown in the figure, the resonance can be easily identified and characterized. The clear change in the behavior of the half-life in Fig. 8 at $R = 2.00\ a_0$ is related to a wide avoided crossing of the parent state ($\tilde{C}$) with state $3\ {}^2A''$, that can be seen in Fig. 5. The half-life, that decreases with R until then, increases slowly in the region of the avoided crossing, up to around $R = 2.35\ a_0$, when it starts to decrease again. The quantum defect also changes its behavior in the region of the avoided crossing, but more smoothly, and then becomes approximately constant above $R = 2.5\ a_0$.

---

[1] M. Dizdaroglu and P. Jaruga, Mechanisms of free radical-induced damage to DNA, Free Radical Research **46**, 382 (2012).

[2] J. McConkey, C. Malone, P. Johnson, C. Winstead, V. McKoy, and I. Kanik, Electron impact dissociation of oxygen-containing molecules-a critical review, Phys. Rep. **466**, 1 (2008).

[3] C. Makochekanwa, K. Oguri, R. Suzuki, T. Ishihara, M. Hoshino, M. Kimura, and H. Tanaka, Experimental observation of neutral radical formation from CH_4 by electron impact in the threshold region, Phys. Rev. A **74**, 042704 (2006).

[4] M. Ziolkowski, A. Vikar, M. Mayes, A. Bencsura, G. Lendvay, and G. Schatz, Modeling the electron-impact dissociation of methane, J. Chem. Phys. **137**, 22A510 (2012).

[5] J. R. Hamilton, J. Tennyson, S. Huang, and M. J. Kushner, Calculated cross sections for electron collisions with NF_3, NF_2 and NF with applications to remote plasma sources, Plasma Sources Sci. Technol. **26**, 065010 (2017).

[6] D. Davis, V. P. Vysotskiy, Y. Sajeev, and L. S. Cederbaum, A one-step four-bond-breaking reaction catalyzed by an electron, Angewandte Chemie International Edition **51**, 8003 (2012).

[7] D. Davis, S. Kundu, V. S. Prabhudesai, Y. Sajeev, and E. Krishnakumar, Formation of CO_2 from formic acid through catalytic electron channel, J. Chem. Phys. **149**, 064308 (2018).

[8] M. J. Jensen, R. C. Bilodeau, O. Heber, H. B. Pedersen, C. P. Safvan, X. Urbain, D. Zajfman, and L. H. Andersen, Dissociative recombination and excitation of H_2O^+ and HDO^+, Phys. Rev. A **60**, 2970 (1999).

[9] Z. Mašín, J. Benda, J. D. Gorfinkiel, A. G. Harvey, and J. Tennyson, UKRmol+: A suite for modelling electronic processes in molecules interacting with electrons, positrons and photons using the R-matrix method, Comput. Phys. Commun. **249**, 107092 (2020).

[10] P. M. Mul, J. W. McGowan, P. Defrance, and J. B. A. Mitchell, Merged electron-ion beam experiments. V. Dissociative recombination of OH^+, H_2O^+, H_3O^+ and D_3O^+, J. Phys. B **16**, 3099 (1983).

[11] S. Datz, R. Thomas, S. Rosén, M. Larsson, A. M. Derkatch, F. Hellberg, and W. van der Zande, Dynamics of Three-Body Breakup in Dissociative Recombination: H_2O^+, Phys. Rev. Lett. **85**, 5555 (2000).

[12] S. Rosén, A. Derkatch, J. Semaniak, A. Neau, A. Al-Khalili, A. Le Padellec, L. Vikor, R. Thomas, H. Danared, M. af Ugglas, and M. Larsson, Recombination of simple molecular ions studied in storage ring: Dissociative recombination of H_2O^+, Faraday Discuss. **115**, 295 (2000).

[13] R. Thomas, S. Rosén, F. Hellberg, A. Derkatch, M. Larsson, S. Datz, R. Dixon, and W. J. van der Zande, Investigating the three-body fragmentation dynamics of water via dissociative recombination and theoretical modeling calculations, Phys. Rev. A **66**, 032715 (2002).

[14] M. Fogle, E. M. Bahati, M. E. Bannister, S. H. M. Deng, C. R. Vane, R. D. Thomas, and V. Zhaunerchyk, Electron-impact dissociation of XH_2^+ (X=B, C, N, O, F): Absolute cross sections for production of XH^+ and X^+ fragment ions, Phys. Rev. A **82**, 042720 (2010).

[15] S. M. Nkambule, Å. Larson, S. Fonseca dos Santos, and A. E. Orel, Theoretical study of the mechanism of H_2O^+ dissociative recombination, Phys. Rev. A **92**, 012708 (2015).

[16] J. Suárez, L. Méndez, and I. Rabadán, Nonadiabatic quantum dynamics predissociation of $H_2O^+(\tilde{B}^2B_2)$, J. Phys. Chem. Lett. **6**, 72 (2015).

[17] J. Suárez, L. Méndez, and I. Rabadán, Nonadiabatic fragmentation of H_2O^+ and isotopomers. Wave packet propagation using ab initio wavefunctions, Phys. Chem. Chem. Phys. **20**, 28511 (2018).

[18] UKRmol+, ukrmol-in version 2.0.2, 2019, https://zenodo.org/record/2630496.

[19] UKRmol+, ukrmol-out version 2.0.1, 2019, https://zenodo.org/record/2630571#.Xns3-4XXLIU.

[20] P. G. Burke, *R-Matrix Theory of Atomic Collisions: Application to Atomic, Molecular and Optical Processes* (Springer, New York, 2011).

[21] F. T. Smith, Lifetime matrix in collision theory, Phys. Rev. **118**, 349 (1960).

[22] J. Tennyson and C. J. Noble, RESON: A program for the detection and fitting of Breit-Wigner resonances, Comput. Phys. Commun. **33**, 421 (1984).

[23] K. Yuan, R. N. Dixon, and X. Yang, Photochemistry of the water molecule: Adiabatic versus nonadiabatic dynamics, Acc. Chem. Res. **44**, 369 (2011).

[24] H.-J. Werner, P. J. Knowles, G. Knizia, F. R. Manby, M. Schütz, P. Celani, W. Györffy, D. Kats, T. Korona, R. Lindh, A. Mitrushenkov, G. Rauhut, K. R. Shamasundar, T. B. Adler, R. D. Amos, A. Bernhardsson, A. Berning, D. L. Cooper, M. J. O. Deegan, A. J. Dobbyn, F. Eckert, E. Goll, C. Hampel, A. Hesselmann, G. Hetzer, T. Hrenar, G. Jansen, C. Köppl, Y. Liu, A. W. Lloyd, R. A. Mata, A. J. May, S. J. McNicholas, W. Meyer, M. E. Mura, A. Nicklass, D. P. O'Neill, P. Palmieri, D. Peng, K. Pflüger, R. Pitzer, M. Reiher, T. Shiozaki, H. Stoll, A. J. Stone, R. Tarroni, T. Thorsteinsson, and M. Wang, MOLPRO, version 2015.1, a package of *ab initio* programs, 2015, http://www.molpro.net.

[25] P. L. Barbieri, P. A. Fantin, and F. E. Jorge, Gaussian basis sets of triple and quadruple zeta valence quality for correlated wave functions, Mol. Phys. **104**, 2945 (2006).

[26] A. Canal Neto, E. Muniz, R. Centoducatte, and F. Jorge, Gaussian basis sets for correlated wave functions. Hydrogen, helium, first- and second-row atoms, J. Mol. Struct (THEOCHEM) **718**, 219 (2005).

[27] T. R. Huet, C. J. Pursell, W. C. Ho, B. M. Dinelli, and T. Oka, Infrared spectroscopy and equilibrium structure of $H_2O^+(\tilde{X}^2B_1)$, J. Chem. Phys. **97**, 5977 (1992).

[28] M. Eroms, M. Jungen, and H.-D. Meyer, Nonadiabatic nuclear dynamics after valence ionization of H_2O, J. Phys. Chem. A **114**, 9893 (2010).

[29] Note that the $OH + H^+$ channel could also correspond to $O + H + H^+$ [8].

[30] L. S. Harbo, S. Dziarzhytski, C. Domesle, G. Brenner, A. Wolf, and H. B. Pedersen, Lifetime of low vibrational levels of the metastable $\tilde{B}\,^2B_2$ state of H_2O^+ probed by photodissociation at 532 nm, Phys. Rev. A **89**, 052520 (2014).

[31] M. J. Seaton, Quantum defect theory, Rep. Prog. Phys. **46**, 167 (1983).

[32] Y. Itikawa and N. Mason, Cross sections for electron collisions with water molecules, J. Phys. Chem. Ref. Data **34**, 1 (2005).

[33] https://edatos.consorciomadrono.es/dataset.xhtml?persistentId=doi:10.21950/LQYPTM.